Research Article

3D-printed Lunar regolith simulant-based geopolymer composites with bio-inspired sandwich architectures

Siqi Ma[a,b], Yuqi Jiang[a,b], Shuai Fu[c], Peigang He[a,b,*], Chengyue Sun[d],
Xiaoming Duan[a,b], Dechang Jia[a,b], Paolo Colombo[e,f], Yu Zhou[a,b]

[a]*Institute for Advanced Ceramics, School of Materials Science and Engineering,
Harbin Institute of Technology, Harbin 150001, China*
[b]*Key Laboratory of Advanced Structural–Functional Integration Materials & Green
Manufacturing Technology, Harbin Institute of Technology, Harbin 150001, China*
[c]*Max Planck Institute for Polymer Research, Mainz 5512, Germany*
[d]*Laboratory for Space Environment and Physical Sciences, Harbin Institute of Technology, Harbin 150001, China*
[e]*Department of Industrial Engineering, University of Padova, Padova 35122, Italy*
[f]*Department of Materials Science and Engineering, The Pennsylvania State University, Philadelphia 16802, USA*

© The Author(s) 2022.

Abstract: Over time, natural materials have evolved to be lightweight, high-strength, tough, and damage-tolerant due to their unique biological structures. Therefore, combining biological inspiration and structural design would provide traditional materials with a broader range of performance and applications. Here, the application of an ink-based three-dimensional (3D) printing strategy to the structural design of a Lunar regolith simulant-based geopolymer (HIT-LRS-1 GP) was first reported, and high-precision carbon fiber/quartz sand-reinforced biomimetic patterns inspired by the cellular sandwich structure of plant stems were fabricated. This study demonstrated how different cellular sandwich structures can balance the structure–property relationship and how to achieve unprecedented damage tolerance for a geopolymer composite. The results presented that components based on these biomimetic architectures exhibited stable non-catastrophic fracture characteristics regardless of the compression direction, and each structure possessed effective damage tolerance and anisotropy of mechanical properties. The results showed that the compressive strengths of honeycomb sandwich patterns, triangular sandwich patterns, wave sandwich patterns, and rectangular sandwich patterns in the *Y*-axis (*Z*-axis) direction were 15.6, 17.9, 11.3, and 20.1 MPa (46.7, 26.5, 23.8, and 34.4 MPa), respectively, and the maximum fracture strain corresponding to the above four structures could reach 10.2%, 6.7%, 5.8%, and 5.9% (12.1%, 13.7%, 13.6%, and 13.9%), respectively.

Keywords: Lunar regolith simulant (LRS); three-dimensional (3D) printing; geopolymer (GP); *in situ* resource utilization (ISRU); bio-inspired patterns; damage tolerance

---

* Corresponding author.

E-mail: Peiganghe@hit.edu.cn

1 Introduction

As the ideal place for future space migration, human exploration of the Moon has increased in recent years [1]. However, due to the high cost and risk of space transportation, Gellert *et al.* [2] and Wang *et al.* [3] consider by using the *in situ* resource utilization (ISRU) approach on the Moon as much as possible for space base construction. The ISRU approach can minimize the cost of space transportation, and thus fully use the mineral resources on the Moon [4]. As a potential alternative to cement, geopolymers have attracted widespread attention due to their low density, low thermal conductivity, and the possibility of using a wide range of raw materials for their fabrication [5,6]. The most outstanding advantage of using geopolymers for the Moon construction is that the raw materials can be obtained from Lunar regolith, avoiding the high transportation costs of transporting cement from the Earth to the Moon (*in situ* synthesis of geopolymers on the Moon can be accomplished with only little quantities of extra materials delivered from the Earth) [5,7,8]. Related studies [5,9] have demonstrated that active substances in Lunar regolith are suitable for geopolymerization, as they provide the necessary Si and Al sources for the thermodynamically favorable formation of amorphous aluminosilicate networks, once subjected to alkaline attack. Based on the above description, at this stage, there is a growing consensus to select Lunar regolith-based geopolymers as the building material for the Moon base [6].

Lightweight, high-strength, and rigid building materials have always been the focus of attention [10–12]. To overcome the inherent brittleness of geopolymers, various reinforcing materials have been adopted, such as chopped fibers [13,14], continuous fiber mats [15,16], and other two-dimensional (2D) materials [17]. Carbon fibers have been widely recognized as an excellent material for their good tensile properties, chemical stability in an alkaline environment, and high-temperature resistance [18,19]. Fiber–geopolymer composites exhibit excellent mechanical properties such as high strength, hardness, and toughness [20]. However, the problem of brittleness exhibited by geopolymer composites remains the greatest obstacle to their use as structural materials [21,22]. In addition, if the intrinsic mechanical properties of geopolymers could be improved, this would enable a significant reduction of the amount of material necessary for achieving a given strength, opening new

development opportunities such as lightweight sandwiches, electronic devices, and catalytic carriers [23,24]. Therefore, besides introducing reinforcing phases to improve the strength and toughness of geopolymers, Compton and Lewis [10] and Ma *et al.* [21] have also attempted to improve the vulnerability of geopolymer materials to catastrophic fracture through extrinsic structural design.

By taking lessons from natural materials, Naleway *et al.* [25] and Zhang *et al.* [26] have found that many biological structures have outstanding mechanical properties and extrinsic toughening abilities. For example, these structures can possess specific strength or toughness values, whose bulk materials with the same volume cannot achieve by reducing their own weight [12,27]. To date, although about 7 million species of living organisms exist on the Earth, the architectures observed in biological materials are remarkably repetitive [28,29]. This is because many organisms have evolved similar solutions to natural challenges such as habitat conditions or predators' characteristics. For example, the typical Bouligand-type pattern (a multi-layered structure with layers arranged at specific angles) was observed in hard areas such as the mantis shrimp forceps, the scales of the tongue fish, and the superficial surface of shells [30]. Moreover, unique cellular sandwich structures can be observed in various plant rhizomes and leafs, ensuring that the nutrient components are smoothly transported to the top through the inside and at the same time, providing specific lodging resistance [31,32]. Inspired by the cellular structure of the rhizome of *Elytrigia repens* and bamboo, Peng *et al.* [33] designed a graphene scaffold pattern with an ultra-light structure. The structure showed excellent mechanical properties at high porosity levels. In this respect, by combining the structural design of composites with biomimetic structures, new horizons will be provided for their applications, especially in saving consumables, reducing labor costs, and improving safety [13,34,35].

Thus, developing geopolymer composite structures with high strength and toughness based on biological inspiration has become the focus of attention in architecture. In this study, common plant cellular sandwich structures were selected for simplification to comprehensively evaluate the effect of biomimetic structure on the mechanical properties of geopolymer composites, and four types of cellular sandwich structures were fabricated: (1) honeycomb, (2) triangular, (3) wave, and (4) rectangular. Notably, combining *in situ* compression experiments with the finite element method

(FEM) analysis, we revealed that the three-dimensional (3D)-printed composites exhibited pattern-dependent mechanical properties, providing a new degree of freedom for designing lightweight structural materials with tailorable strength and fracture tolerance.

2   Materials and methods

2. 1   Preparation of Lunar regolith simulant

The Lunar regolith simulant (HIT-LRS-1) prepared for this study was designed to simulate the regolith of the Maria geological terrain of the Moon. Reference [36] indicated that the composition of the regolith in this geological terrain is highly consistent with that of the JSC-1A Lunar regolith simulant. Therefore, the JSC-1A simulant was selected as a reference for the preparation of HIT-LRS-1. The raw materials for the fabrication of HIT-LRS-1 included basalt powder (Hebei Runhuabang New Material Technology Co., Ltd., China), plagioclase powder (Shijiazhuang Shuoheng New Material Technology Co., Ltd., China), forsterite powder (Henan YanXi Mineral Products Co., Ltd., China), albite powder (Shijiazhuang Shuoheng New Material Technology Co., Ltd., China), ilmenite powder (Qinghe County Benyu Metal Material Co., Ltd., China), hematite powder (Shanghai Macklin Biochemical Co., Ltd., China), silica powder (Shanghai Macklin Biochemical Co., Ltd., China), alumina powder (Shanghai Macklin Biochemical Co., Ltd., China), and cristobalite powder (Shanghai Macklin Biochemical Co., Ltd., China) [37]. The main chemical compositions of the Lunar regolith simulant are based on SiO_2, Al_2O_3, Fe_2O_3, MgO, Na_2O, TiO_2, etc., and the content of the amorphous phase is about 30% or more [8]. The Lunar regolith simulant synthesis is referred to Refs. [38,39]: (1) Basalt is the main mineral component in the regolith, mainly providing a source of silicon and aluminum. (2) Fe_2O_3 in the Lunar regolith simulant is mainly provided by hematite. (3) Other mineral components in the simulant are delivered by plagioclase, albite, and ilmenite. (4) The amorphous component of the simulant can be provided by various minerals and additional introduced amorphous silica and alumina. First, powders of basalt (40 wt%), plagioclase (20 wt%), forsterite (10 wt%), albite (5 wt%), ilmenite (5 wt%), hematite (5 wt%), silica (5 wt%), alumina (5 wt%), and cristobalite (5 wt%) were sieved through an 80-mesh sieve. Then, these powders and 100 mL of ethanol were transferred together with 1000 g ZrO_2 grinding balls (5 mm in diameter) into polyurethane grinding jars for ball-milling 2 h at 400 r/min under 25 ℃, as shown in Fig. 1. Afterward, the mixture was separated from the grinding balls and dried in an oven (80 ℃, 24 h) to obtain HIT-LRS-1 powder.

As shown in the X-ray diffraction (XRD) results (Fig. 2(a)), the resulting HIT-LRS-1 is mainly composed of pyroxene, forsterite, feldspar, albite, olivine, trevorite, and oxides (mineral composition consistent with JSC-1A simulant, e.g., pyroxene, forsterite, feldspar, albite, and olivine [36]). Figures 2(b) and 2(c) present the scanning electron microscopy (SEM) image and elemental mappings of the resulting HIT-LRS-1 powder, respectively, confirming the presence of Al, Si, O, Na, K, Mg, Ca, Fe, C, Ti, Ni, and Cr elements. The primary elemental composition of this simulant reveals that it possessed the main components suitable for the formation of synthetic geopolymers, in particular Si and Al. The composition analysis in Table 1 indicates that the oxides in the resulting Lunar regolith simulant
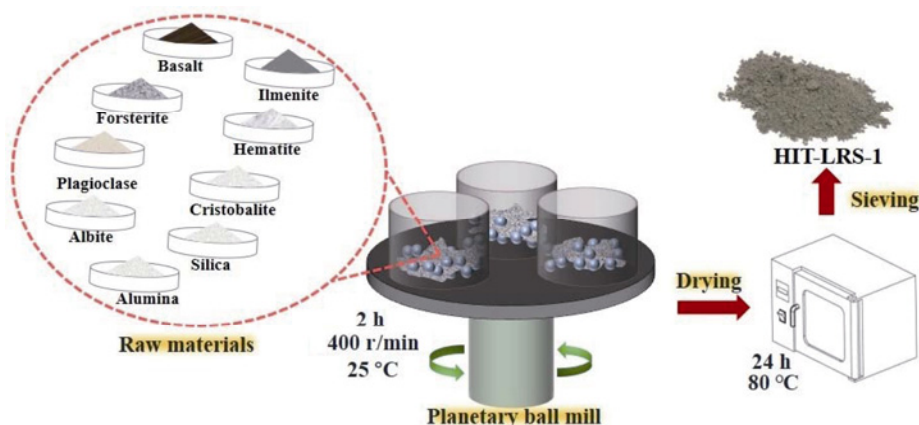

Fig. 1   Schematic illustration of the preparation of HIT-LRS-1.
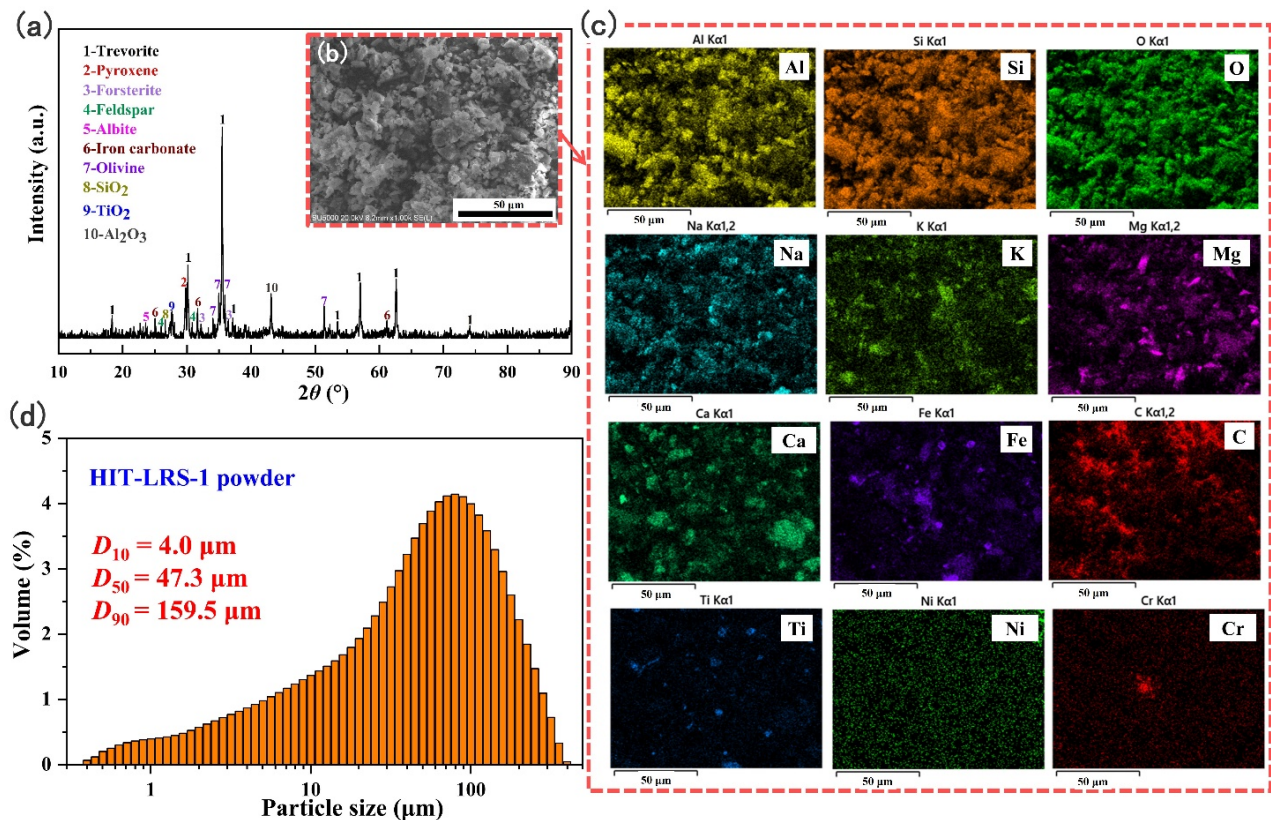
Fig. 2 (a) XRD patterns of HIT-LRS-1 powder. (b) SEM image of HIT-LRS-1 powder. (c) Energy dispersive spectroscopy (EDS) mappings of the whole area in (b). (d) PSD of the resulting HIT-LRS-1 powder.

Table 1 Major oxide compositions of HIT-LRS-1 in comparison with those of the other Lunar regolith simulants and the averages of Apollo 12, 16, and 17 missions (wt%)

	SiO_2	Al_2O_3	Fe_2O_3	FeO	MgO	CaO	Na_2O	K_2O	TiO_2	P_2O_5	Other	Ref.
HIT-LRS-1	45.91	14.06	11.64	~0	10.15	7.23	4.36	2.24	1.85	0.74	1.82	This work
Apollo 12	46.30	12.90	~0	15.10	9.30	10.70	0.47	0.16	3.00	0.40	1.67	[42]
Apollo 16	45.00	27.30	~0	5.10	5.70	15.70	0.46	0.14	0.54	~0	0.06	[40]
Apollo 17	42.20	15.70	~0	12.40	10.30	11.50	0.20	0.10	5.10	~0	2.50	[36]
JSC-1A	44.60	15.14	11.52	~0	8.21	9.70	3.06	0.78	1.70	0.59	4.70	[40]
JSC-2A	43.38	18.30	15.02	~0	3.82	11.47	3.14	0.98	2.32	0.69	0.88	[43]
EAC-1	42.00	10.00	14.00	~0	13.00	11.00	2.70	1.00	2.30	0.70	3.30	[44]

mainly include SiO_2, Al_2O_3, Fe_2O_3, MgO, CaO, and Na_2O. It can be deduced that the prepared Lunar regolith simulant is consistent with Refs. [40,41], reporting the oxide composition of different simulants and actual Lunar regolith. As shown in Fig. 2(d), the particle size distribution (PSD) of the as-prepared HIT-LRS-1 powder ranged from 0.31 to 391 μm (D_{10} = 4.0 μm, D_{50} = 47.3 μm, and D_{90} = 159.5 μm, where D means the particle diameter), which was similar to the powder size distribution of JSC-1A [40]. The amount of amorphous phase in HIT-LRS-1 was estimated to be around 29.2± 1.6 wt%, in agreement with Ref. [40] (amorphous phase content measurement method: (1) Weigh 1 g of HIT-LRS-1

powder into 1 L of 10 mol/L NaOH solution; (2) filter and dry that mixed solution after magnetic stirring for 12 h; (3) calculate the quality loss); it should be noted that it is this fraction that is capable of forming a geopolymer upon contact with an alkaline solution.

2. 2　3D printing of Lunar regolith simulant-based geopolymer inks

Raw materials selected for preparing short carbon fiber/ quartz sand@Lunar regolith simulant-based geopolymer (C_{sf}/QS@HIT-LRS-1 GP) inks included chopped short carbon fiber with an average length of 600 μm and a

diameter of 5.3 μm (Jilin Carbon Co., Ltd., China), NaOH (85 wt%, Tianjin Guangfu Technology Development Co., Ltd., China), sol–silica (40 wt%, Qingdao Mike Silica Gel Desiccant Co., Ltd., China), and quartz sand (Henan Haizhina Environmental Protection Technology Co., Ltd., China). Figure 3 illustrates the synthesis of the C_{sf}/QS@HIT-LRS-1 GP ink for direct ink writing (DIW). First, the alkaline silicate solution was papered by adding NaOH (8.3 g) to the sol–silica (30 g) under magnetic stirring for 72 h. Afterward, HIT-LRS-1 powder (30 g) and alkaline silicate solution were mixed under stirring at 0 ℃ for 20 min to form a Lunar regolith simulant-based GP ink. This was followed by adding carbon fiber (volume fraction (α) ≈ 0.50, 0.75, 1.00, and 1.25 vol%) and quartz sand (mass fraction (ω) ≈ 10, 20, 30, 40, 50, and 60 wt%) as reinforcements to form C_{sf}/QS@HIT-LRS-1 GP inks under ultrasound-assisted stirring (quartz sand is to be considered as a fine aggregate, which could be substituted by crushed Lunar rocks in the future). Finally, the C_{sf}/QS@HIT-LRS-1 GP ink was inserted into a 30 mL plastic charging cylinder with a 0.82 mm diameter needle, and the ink-writing process was carried out according to what has been described in detail in Ref. [45]. Once the slurry has been injected into the plastic cylinder, the cylinder should be placed in a centrifuge for centrifugal shaking to ensure that the slurry is adequately filled. Specifically, the printing speed selected for this printing process was 40 mm/s, the printing pressure was ranged from 70 to 80 psi, the printing platform temperature was set to be 25 ℃, and the print layer slice thickness was 0.76 mm (the thickness of the slice was slightly less than the diameter of the nozzle to ensure that the two adjacent layers were fully overlapped). It should be noted that the printed samples were cured at room temperature for 7 d and in an oven at 60 ℃ for 2 d before characterization and test.

2. 3 Design of biomimetic structures

The sandwich structures refer to the natural cellular structures commonly observed in *Elytrigia repens* and other herbaceous plants, as shown in Fig. 4(a). *Elytrigia repens* exhibits a high lodging resistance capability because of the numerous irregular polygonal holes between the inner and outer walls of its rhizomes, which act as energy absorbers and shock absorbers when the branches are struck and bent [31]. The porous energy-absorbing structures presented in the rhizomes provide a reference for the design of toughened structures, but such pore structures are irregular and therefore difficult to reproduce. Inspired by the irregular cellular sandwich structures in the *Elytrigia*, four regular cellular sandwich architectures were constructed, including (1) honeycomb (Fig. 4(b)), (2) triangular (Fig. 4(c)), (3) wave (Fig. 4(d)), and (4) rectangular (Fig. 4(e)). The typical morphology of each sample was observed by using an SEM to evaluate the printing accuracy of these sandwich structures. The dimension parameters of the honeycomb sandwich structure (B1) and the SEM images of the samples are shown in Fig. 4(b). The filament width (W), single height (L_1), and included angle (θ) of the honeycomb cellular were 0.78 mm, 1.60 mm, and 30°, respectively. Figures 4(b1) and 4(b2) (the red circles) show detailed features of the central region and the line transition region of the honeycomb structure, respectively. It can be observed that the honeycomb structure had a regular shape and flat surfaces without defects. As shown in Fig. 4(c), the W, outer height (L_2), and inner height (L_3) in the triangular sandwich structure were 0.81 mm, 2.40 mm,
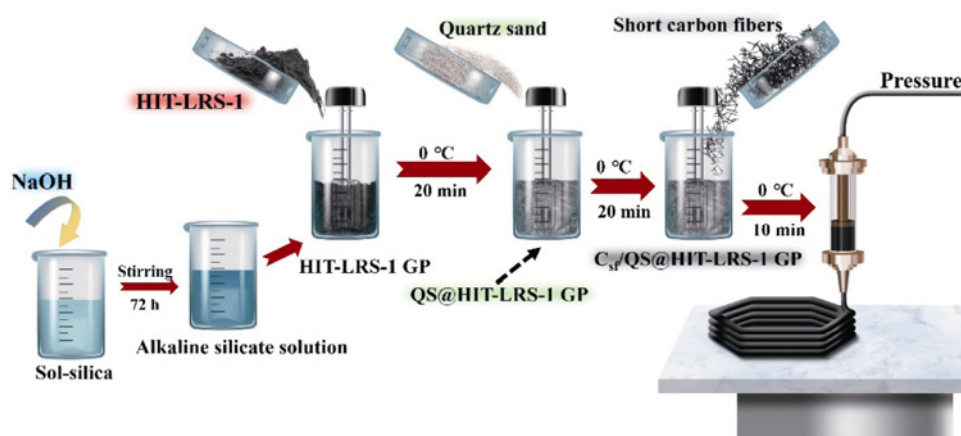

Fig. 3　Schematic illustration of DIW of HIT-LRS-1 geopolymer inks.
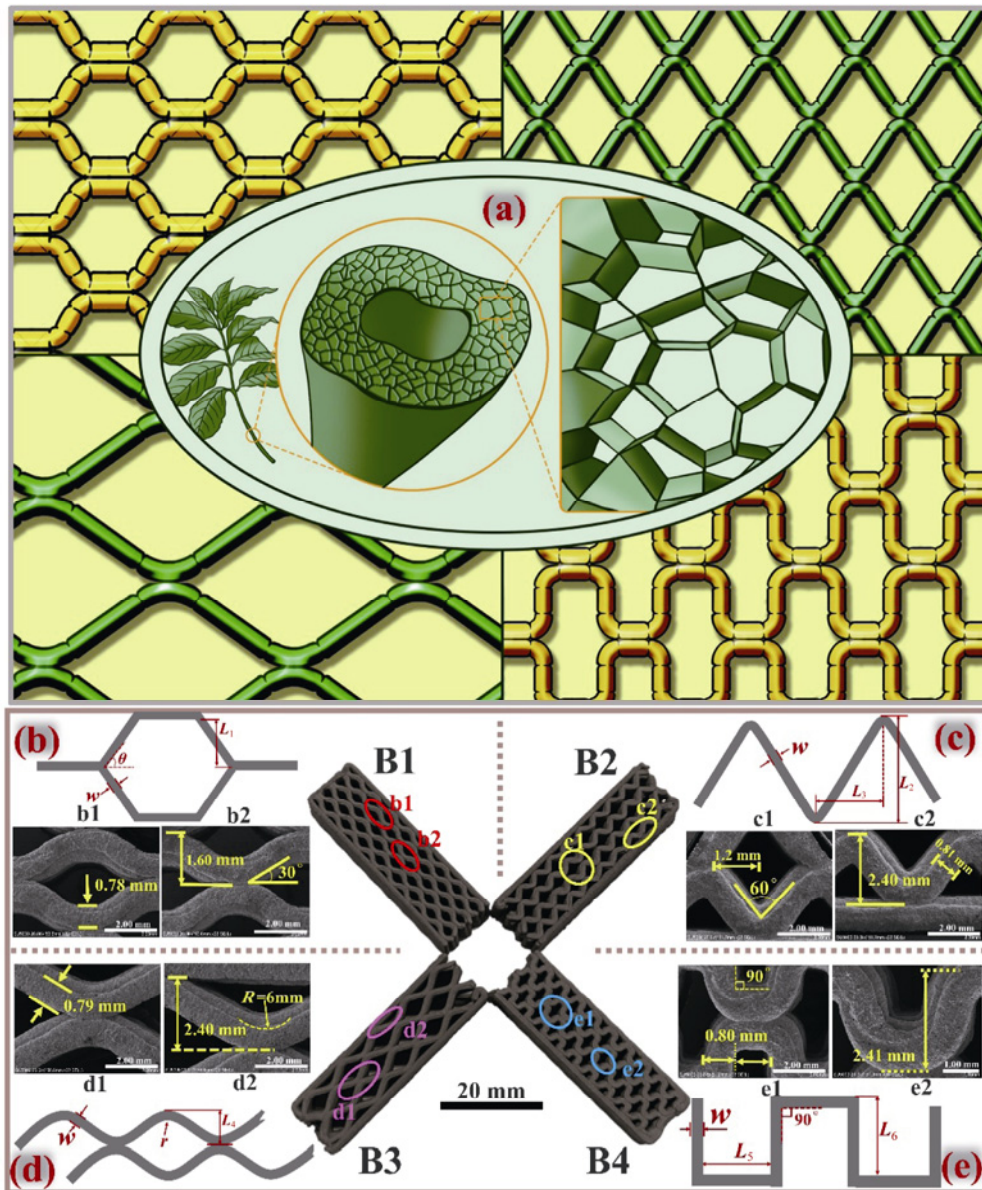
Fig. 4 (a) Schematic diagram of inspiration sources. Photo and microscopic images of 3D-printed C_{sf}/QS@HIT-LRS-1 GP sandwich structures: (b) macroscopic images of 3D-printed geopolymer products with a honeycomb sandwich structure (B1); (c) microscopic images of 3D-printed geopolymer products with a triangular sandwich structure (B2); (d) microscopic images of 3D-printed geopolymer products with a wave sandwich structure (B3); and (e) microscopic images of 3D-printed geopolymer products with a rectangular sandwich structure (B4).

and 1.20 mm, respectively. It can be seen from Figs. 4(c1) and 4(c2) (the yellow circles) that the triangular sandwich structure had a clear profile and excellent filament overlap. Figures 4(d1) and 4(d2) (the purple circles) are the SEM images of the constituent elements of the wave sandwich structure, and it could be observed that the W in the wave structure was still 0.79 mm, which is consistent with the design dimensions (0.80 mm). Other dimensions of significance, such as height (L_4) and arc radius (r), were 2.40 and 6.0 mm, respectively. The microstructures of the rectangular

sandwich structure (Figs. 4(e1) and 4(e2)) (the blue circles) reveal that the design filament width (W) of the structure was about 0.80 mm, and the transition region of the rectangular structure had excellent continuity and high formability. The inner width (L_5) and outer height (L_6) of the rectangular unit were 0.80 and 2.41 mm, respectively. In summary, the high spatial resolution of the four printed sandwich structures indicated that the developed 1C_{sf}/20QS@HIT-LRS-1 GP ink could meet the requirements of high-precision writing.

2. 4 Characterization

The rheological properties of HIT-LRS-1 GP ink were characterized by a discovery hybrid rheometer (Discovery HR 30, TA Instruments, USA) at 25 ℃ with a flat steel plate geometry of 10 mm and a gap of 1 mm. The apparent viscosity of GP slurries was tested as a function of shear rate ranging from 10^{-2} to 10^{1} s^{-1} (steady rate sweep), and the storage modulus (G')/loss modulus (G'') were tested as a function of stress ranging from 10^{0} to 10^{4} Pa under 1 Hz (dynamic oscillation tests). The trend in apparent viscosity with the increasing shear rate was measured to verify that the slurry has shear thinning properties (only slurries with shear thinning properties can be employed with the DIW technology), while the modulus was measured to verify that the slurry could transition from a pseudo-plastic to a quasi-liquid state upon the application of shear stress (τ, in Pa). The millimeter structures in the printed structures were clearly scanned by the SEM (SU5000, FEI, Japan). The flexural and compressive strengths of extruded rods (four samples) and printed sandwich panels (four samples) were tested by using a universal testing machine (AG-IS/AG-Xplus, Shimadzu, Japan) at 0.5 mm/s. The sample dimensions were 36 mm × 4 mm × 3 mm for the rods and 40 mm × 12.5 mm × 12.5 mm for the sandwich panels. The peaks of the stress–strain curves were taken as the compressive strengths of the 3D-printed samples. The reported mechanical properties represent an average of at least four samples. The PSD of the resulting HIT-LRS-1 powder was measured on a laser particle size analyzer (Mastersizer 2000 instrument, Malvern, UK) with ethanol as the dispersant. The theoretical density (ρ) was tested by a true density analyzer (TD 2200Q, Beijing builder electronic technology Co., Ltd., China) on finely milled printed structures. The Young's modulus and Poisson's ratio were tested by using a Young's modulus and damping analyzer (RFDA-HTVP-1750C, IMCE, Belgium). To further elucidate the effect of different cellular shapes on the mechanical

behavior of each structure, the FEM analysis was chosen to analyze the failure behavior of each structure. The FEM analysis was conducted by ANSYS 2019 software (American ANSYS Corporation, USA) based on the 3D structures modeled by SolidWorks2018 software. We attributed the same Young's modulus, ρ, and Poisson's ratio to the four bio-inspired sandwich patterns, and employed the same boundary condition to simulate their compressive strengths (Table 2). In all cases, the bottom surface of the structure was fixed, and the stress was applied from the top surface (1000 N, corresponding to the elastic deformation stage of all sandwich structures).

3 Results and discussion

3. 1 Rheological properties of HIT-LRS-1 GP inks

The rheological properties of the ink are the critical factor in determining whether it could be printed smoothly [46,47]. The apparent viscosity, G', G'', and yield stress (τ_0, in Pa) of the ink were evaluated to describe the printability of the ink quantitatively. An ink suitable for DIW needs to have a shear thinning behavior, in which the apparent viscosity gradually decreases as the shear rate increases (which enables the ink to be smoothly and continuously extruded), and a high G' in a steady state (which enables the ink to maintain its shape after extrusion and support the deposition of subsequent neighboring filaments). Figure 5(a) shows the apparent viscosity of the five HIT-LRS-1 GP inks with different quartz sand and carbon fiber contents as a function of shear rate (from 10^{-2} to 10^{1} s^{-1}). The apparent viscosity of the inks with different contents of quartz sand (or carbon fiber) decreased as the shear rate increased. It is worth noting that the initial viscosity of the HIT-LRS-1 GP ink without quartz sand and carbon fibers is low (the black curve), being only 199 Pa·s. After the addition of quartz sand, the initial viscosity of each ink increased

Table 2   Basic parameters of the four sandwich structures

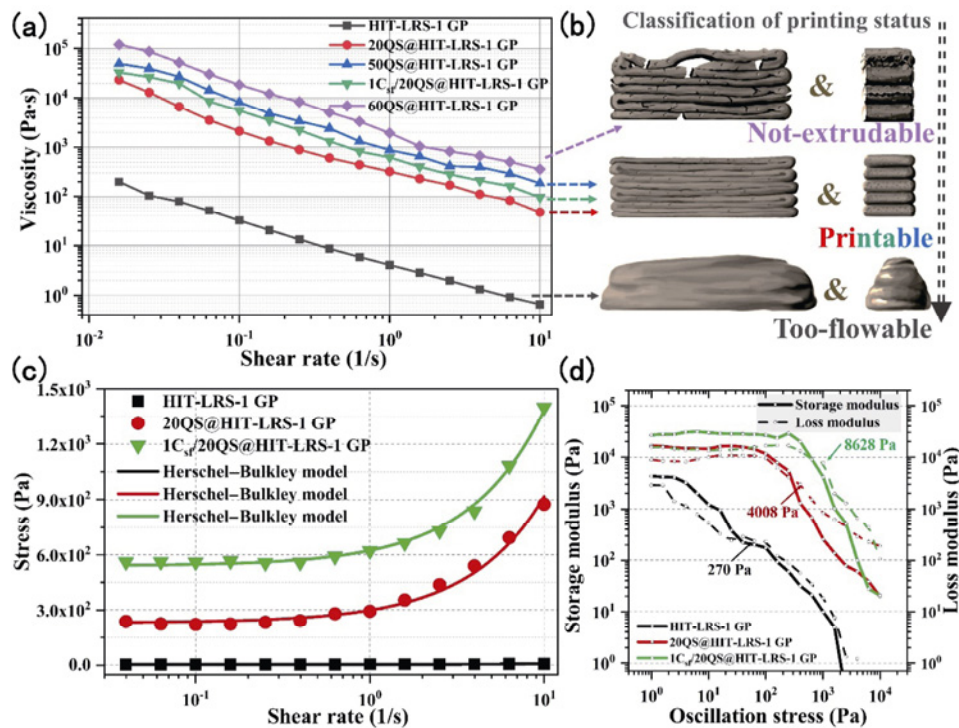| Structure	B1-honeycomb	B2-triangular	B3-wave	B4-rectangular
Young's modulus (GPa)	26	26	26	26
Poisson's ratio	0.21	0.21	0.21	0.21
ρ (g/cm^3)	3.04	3.04	3.04	3.04
Actual volume (mm^3)	40 × 12.5 × 12.5 = 6250	6250	6250	6250
Actual mass (g)	10.91±0.75	10.15±0.54	9.07±1.01	11.90±0.97
Total porosity (%)	42.56±0.04	46.58±0.03	52.23±0.05	37.36±0.04

Fig. 5 Determination of viscosity parameters. (a) Viscosity as a function of shear rate. (b) Schematic visualization of ink printability. (c) Stress as a function of shear rate. The solid lines correspond to the non-Newtonian fluid Herschel–Bulkley (H–B) model describing the stress–shear rate relationship for HIT-LRS-1 GP inks with different quartz sand and carbon fiber contents. (d) Variation curve of shear modulus with oscillation stress.

by 2–3 orders of magnitude, and the initial viscosity of the QS@HIT-LRS-1 GP inks with 20 wt% (the solid red line), 50 wt% (the solid blue line), and 60 wt% (the solid purple line) quartz sand were 23,339, 49,686, and 120,027 Pa·s, respectively. Moreover, the $1C_{sf}$/20QS@HIT-LRS-1 GP ink with the addition of 1.00 vol% carbon fiber and 20 wt% quartz sand also exhibited a higher initial viscosity of approximately 33,279 Pa·s. Figure 5(b) reports a visualization of the macroscopic behavior of different inks. The HIT-LRS-1 GP ink without quartz sand (or carbon fibers) showed a poor layering effect after printing, and its extrusion was accompanied by the overall collapse due to its low τ_0 and viscosity. When an appropriate content of quartz sand (or carbon fibers) was added, the increase in τ_0 and ink viscosity significantly improved the printability of HIT-LRS-1 GP inks, such as 20QS@HIT-LRS-1 GP, 50QS@HIT-LRS-1 GP, and $1C_{sf}$/20QS@HIT-LRS-1 GP (the outline of a printed sample from the three inks was analyzed, and a clear transition between the neighboring layers was observed). As the quartz sand content continued to increase, the 60QS@HIT-LRS-1 GP ink became too viscous to be smoothly extruded and obtain a well-controlled shape, resulting in the ink not being printable. The excessive introduction of non-

reactive substances such as quartz sand will also inhibit the geopolymerization reaction, and thus affect the mechanical properties of the geopolymer composites [48].

To accurately predict the effect of different quartz sand and carbon fiber contents on the initial viscosity of HIT-LRS-1 GP ink and its minimum extrusion stress (minimum τ_0), the H–B model [49] was selected to fit the stress–strain curves of HIT-LRS-1 GP, 20QS@HIT-LRS-1 GP, and $1C_{sf}$/20QS@HIT-LRS-1 GP inks in Fig. 5(c). The expression for the H–B model is as Eqs. (1) and (2):

$$\tau = \tau_0 + m\gamma^n \tag{1}$$

$$\eta = \frac{3m}{n+2}\left(\gamma_{max}\right)^{n-1} \tag{2}$$

where γ is the shear rate (s^{-1}), γ_{max} is the maximum shear rate (s^{-1}), η is the plastic viscosity (Pa·s), m is the consistency coefficient (Pa·s), and n is the flow index of the fluid.

In Table 3, the fitting of the 20QS@HIT-LRS-1 GP and $1C_{sf}$/20QS@HIT-LRS-1 GP inks obtained higher goodness-of-fit (R^2 close to 1), which indicates that introducing a reinforcement in the HIT-LRS-1 GP ink was not detrimental but rather beneficial to its pseudoplastic characteristics. Meanwhile, the theoretical τ_0 and initial viscosity (η) obtained by the H–B model

Table 3 Comparison of rheological coefficients of HIT-LRS-1 GP with different quartz sand or carbon fiber contents fitted by the H−B model

Specimen	H–B model		
	τ_0 (Pa)	η (Pa·s)	R^2
HIT-LRS-1 GP	3.920	0.280	0.952
20QS@HIT-LRS-1 GP	229.900	68.700	0.987
1C$_{sf}$/20QS@HIT-LRS-1 GP	539.200	84.300	0.995

followed the trend of the experimental results (the addition of quartz sand or carbon fiber significantly increased the τ_0 and apparent viscosity of the ink).

To quantitatively describe the changes in the rheological properties of the HIT-LRS-1 GP, 20QS@HIT-LRS-1 GP, and 1C$_{sf}$/20QS@HIT-LRS-1 GP inks, the G' (the solid lines in Fig. 5(d)) and G'' (the dashed lines in Fig. 5(d)) are recorded in the range of 10^0–10^5 Pa. τ_0 values (i.e., the critical values for triggering the liquid–solid transition of HIT-LRS-1 GP inks) were calculated by determining the intersection point for the G' and G'' curves (Fig. 5(d)). The G' is correlated to the amount of energy stored due to elastic deformation when the ink is deformed, and the G'' is correlated to the amount of energy lost due to the viscous deformation of the ink. When the G' is much greater than the G'', the ink mainly undergoes elastic deformation, and the corresponding ink is in the solid state. When the G'' is much higher than the G', the ink mainly undergoes viscous deformation, and the corresponding ink is in the liquid state [50]. When the G' and the G'' are equal, the ink is in a semi-solid state, which also means that the intersecting point of the two modulus curves corresponds to the τ_0 of the ink, which is changing its behavior from solid to liquid. The τ_0 of the filler-free HIT-LRS-1 GP ink was only 270 Pa, while the τ_0 for the 20QS@HIT-LRS-1 GP and 1C$_{sf}$/20QS@HIT-LRS-1 GP inks were 4008 and 8628 Pa, respectively. The enhanced τ_0 in HIT-LRS-1 GP inks facilitated the smooth extrusion of HIT-LRS-1 GP inks and subsequent rapid solidification of the extruded filaments. The data discussed above triggered our further exploration of the effect of different carbon fiber contents on the mechanical properties of xC$_{sf}$/20QS@HIT-LRS-1 GP composites.

3. 2 Effect of carbon fiber content on fiber alignment and flexural strength of xC$_{sf}$/20QS@HIT-LRS-1 GP composites

The degree of spatial orientation of chopped fibers with a high aspect ratio (β) during ink extrusion is determined by such parameters as the α and the β of fibers. Kanarska *et al*. [51] clarified the constraint effect of a rod (i.e., short fiber) in a narrow channel by modifying the standard model of the rod motion in a non-Newtonian fluid, and Perez *et al*. [52] predicted the effect of the amount of rods and the β on the degree of directional arrangement during the extrusion process by using a macro-scale continuous model. As shown in Fig. 6(a), the suspension of chopped carbon fibers in a geopolymer ink can be divided into three states, namely a concentrated regime ($1/\beta < \alpha$), a diluted regime ($\alpha < 1/\beta^2$), and a semi-concentrated regime ($1/\beta^2 < \alpha < 1/\beta$). In this work, the α was chosen to be within the range of 0.5–1.25 vol%, while the β was 107 (the average fiber length (F_l) = 567 μm divided by diameter (d) = 5.3 μm). Therefore, taking into account the above parameters, the relationship between β and α in HIT-LRS-1 GP inks was $1/\beta < \alpha$, and the suspension state of the fibers in the inks corresponded to the concentrated regime. According to Ref. [51], when the fiber distribution is in the concentrated regime, and the ratio of the F_l to the needle diameter (ϕ) is 0.67, the fibers would present the ideal oriented arrangement during extrusion. The schematic diagram of the extrusion process of the fibers with the ink is shown in Fig. 6(b). It can be observed that the fibers showed an excellent directional arrangement (the blue area) at the needle position [10], i.e., the arrangement direction of the fibers was parallel to the extrusion direction. Therefore, the fibers would then possess a unidirectional spatial arrangement along the printing direction in the obtained printed sample.

When the short carbon fiber had theoretically been well aligned within the 20QS@HIT-LRS-1 GP matrix, we evaluated the effect of different short carbon fiber contents on the flexural strengths of xC$_{sf}$/20QS@HIT-LRS-1 GP composites (Fig. 6(c)). With the increase of the fiber content, the flexural strength of the samples showed an increasing trend at first, and then a slight decrease. When the carbon fiber content in the sample was 1.00 vol%, the flexural strength of the corresponding 1C$_{sf}$/20QS@HIT-LRS-1 GP sample reached a maximum of 41.6 MPa. The flexural strength of the 1C$_{sf}$/20QS@HIT-LRS-1 GP sample was increased by 50.7% compared to the flexural strength of the composite without carbon fibers, which was only 27.6 MPa. When analyzing the fracture morphologies of the printed samples (Fig. 6(d)), with the increasing fiber
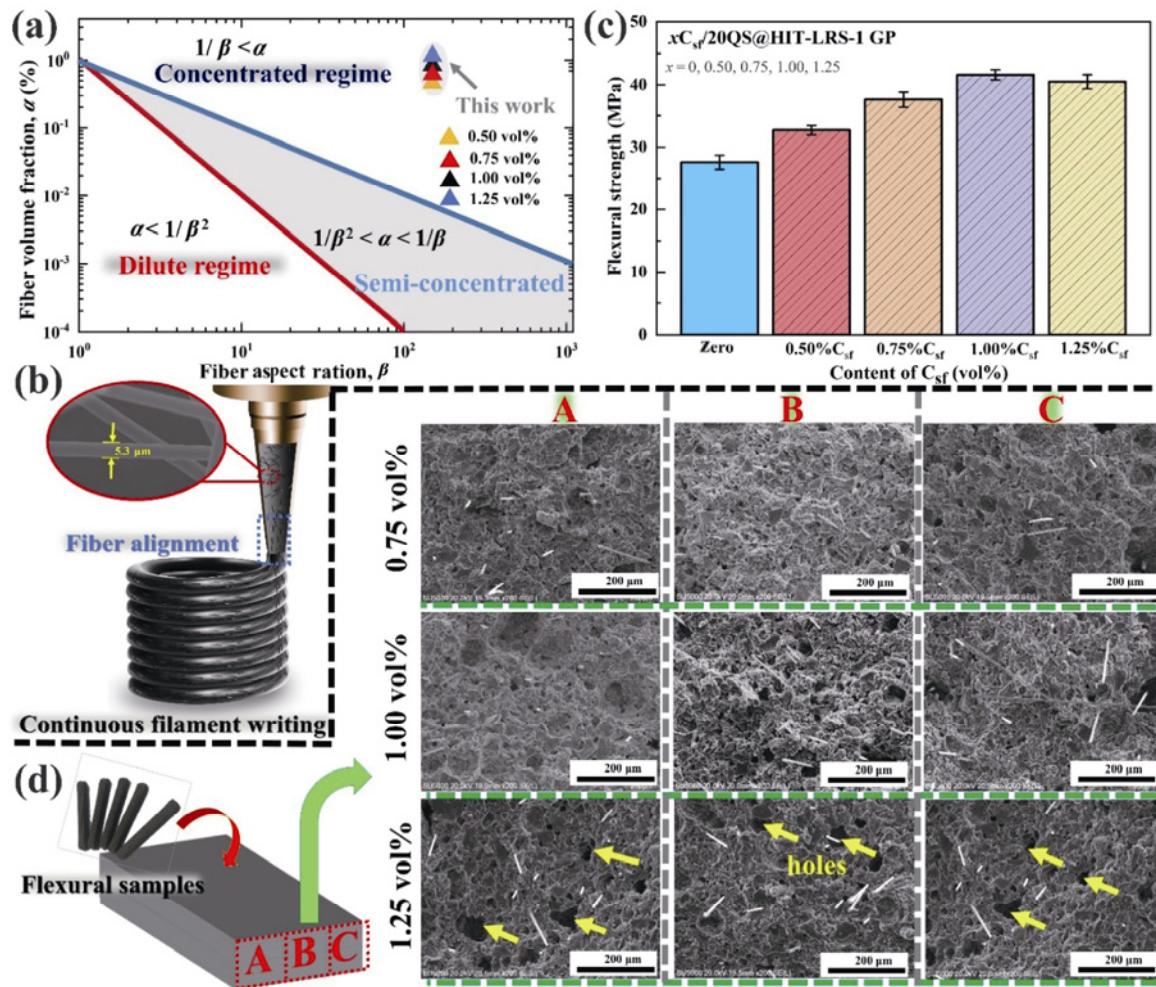
Fig. 6 Description of fiber orientation arrangement. (a) Classifications of fiber suspensions according to α vs. β. (b) Schematic illustration of progressive alignment of high-β short fibers within the nozzle during composite ink deposition. (c) Effect of carbon fiber content on flexural strengths of composites. (d) Fracture surfaces of printed xC$_{sf}$/20QS@HIT-LRS-1 specimens with different contents of carbon fibers.

contents (0.75–1.25 vol%), the fibers showed a better directional arrangement in different regions (A, B, and C regions) inside the sample, indicating that the selected carbon fiber content and length–diameter ratio were appropriate. The carbon fibers with the optimal directional arrangement in the composite during the fracture process would provide a significant pull-out effect, which is also the key to obtaining good mechanical properties of the 1C$_{sf}$/20QS@HIT-LRS-1 GP composite. However, with the increase in fiber content, the number of pores in the sample gradually increased when the fiber content was 1.25 vol%. Many pore defects (the yellow arrows) were formed in the matrix (Fig. 6(d)), probably because the high fiber content and associated viscosity increase did not allow for an adequate deairing of the ink, leading to significant residual porosity and finally reduced

mechanical properties. Therefore, due to its optimal mechanical properties, the 1C$_{sf}$/20QS@HIT-LRS-1 GP ink was selected for the subsequent biomimetic structure design of components.

3.3 Comparison of mechanical properties and fracture behavior of bio-inspired sandwich patterns in different compression directions

Figure 7(a) shows the stress–strain curves for the compression test carried out on the four sandwich structures in the *Y*-axis direction; they all appear to have a non-catastrophic fracture behavior under compression. The stress–strain curves can be divided into three stages, namely linear elastic stage, plateau stage, and compression stage. This indicates that the sandwich samples possessed a pseudo-plastic fracture characteristic that was not present in the geopolymer

material, i.e., such sandwich structures ensure that the component does not collapse when impacted by an external force [53,54]. A similar behavior is also typical of cellular structures (e.g., foams) composed of brittle materials [55,56]. Thus, the occurrence of this ductile fracture behavior may enable the parts to be considered for applications, where the brittle fracture behavior of the geopolymer is not suitable. The compressive strengths of the 3D-printed $1C_{sf}/20QS@HIT\text{-}LRS\text{-}1$ GP composites with honeycomb, triangular, wave, and rectangular sandwich structures were found to be 15.6, 17.9, 11.3, and 20.1 MPa, respectively (Fig. 7(b)). The maximum fracture strain for all of the four sandwich structures were above 5%, as the honeycomb sandwich structure displaying was the highest, of about 10.2%; while the maximum fracture strain of the wave sandwich structure was the lowest, and it could still reach 5.8%. This proves that the four types of geopolymer-based sandwich structures also have promising applications in future building structures, such as exterior protection structures in buildings for vibration damping and energy absorption. The compression snapshots in Figs. 7(c)–7(f) show that when the sandwich structures were subjected to the load, the collapse of the structure would be accompanied by microcracks, and that the four sandwich structures could still maintain a certain degree of structural integrity under compression. The honeycomb (Fig. 7(c)) and rectangular sandwich structures (Fig. 7(f)) showed only the development of minor cracks and local fractures, as compared to the wave sandwich structure (Fig. 7(e)), where large-scale fracture already occurred inside the component when the strain reached 5%. Therefore, it can be inferred that in terms of damage tolerance, the wave sandwich structure was worse than the honeycomb and the triangular ones.

The FEM analysis combined with the observation of crack development was applied to further assess the fracture mechanism of the four sandwich structures. First, the deformation of different regions in each structure was analyzed by the FEM method after applying the stress. When a pressure of 1000 N was applied, the amount of deformation in the Y-axis and Z-axis direction of each structure remained at a relatively low value (all less than 0.1 mm) except for the larger deformation of the wave sandwich (Fig. 8(a)). It can be deduced that the wave structure is slightly inferior to the other three sandwich structures in the Y-axis and Z-axis load bearing capacity, as also observed when carrying out the compression test (Fig. 7(b)). Meanwhile, it can be seen that for the same structure, the compressive deformation in the Z-axis direction
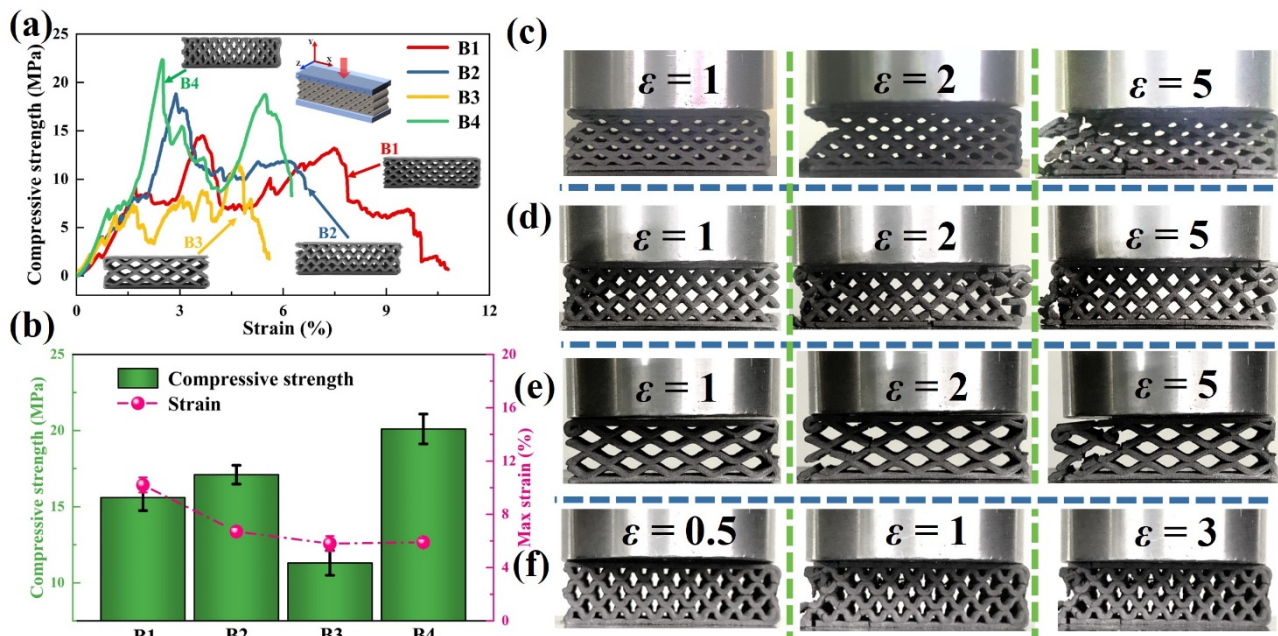

Fig. 7 Mechanical properties of 3D-printed $1C_{sf}/20QS@HIT\text{-}LRS\text{-}1$ GP components in the Y-axis direction. (a) Stress–strain curves of the four sandwich structures during the compression test. (b) Comparison of compressive strength and maximum deformation for the four patterns. (c–f) Photographs of the samples with honeycomb, triangular, wave, and rectangular sandwich patterns at different stages of the compression test (ε is the strain).
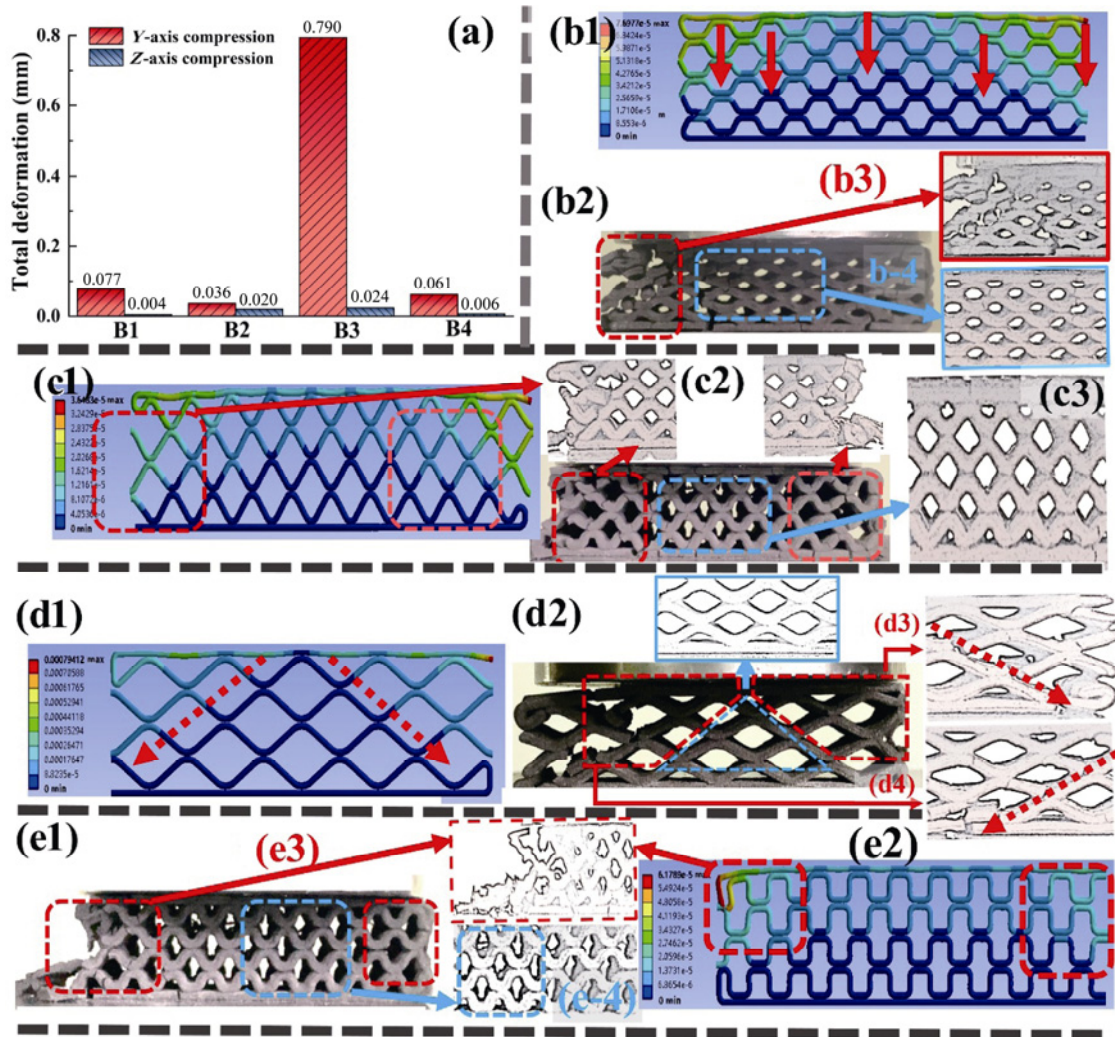
Fig. 8 Fracture mechanism analysis of honeycomb, triangular, wave, and rectangular sandwich structures under quasi-static crushing. (a) Comparison of total deformation of different biomimetic structures by the FEM. (b) Local stress analysis of honeycomb structure during compression and photographs of fractured honeycomb sandwich structure. (c) Local stress analysis of triangular structure during compression and photographs of fractured triangular sandwich structure. (d) Local stress analysis of wave structure during compression and photographs of fractured wave sandwich structure. (e) Local stress analysis of rectangular structure during compression and photographs of fractured rectangular sandwich structure.

(the blue bar) was significantly lower than that in the *Y*-axis direction (the red bar), which means that each structure had a stronger crush resistance in the *Z*-axis direction than that in the *Y*-axis direction (the larger the deformation of the structure, the lower the compressive strength is). From the FEM analysis (Figs. 8(c1), 8(d1), and 8(e2)), we can notice that when the sandwich structure was subjected to *Y*-axis crushing, each structure exhibited a typical crushed zone and a non–crushed zone. For example, when the pressure was applied on the honeycomb sandwich structure (Fig. 8(b1)), the interior of the sample presented a top-down deformation zone, i.e., the pressure transfer in the structure was vertically distributed from top to bottom (the red

arrow). The above discussion could be further validated by analyzing the fractured honeycomb sandwich, where the collapse was observed on both sides of the honeycomb (Fig. 8(b2), the dashed red line in Fig. 8(b3)), while structural integrity was observed in the central region (the blue border in Fig. 8(b4)). Moreover, a similar fracture behavior also occurred in the triangular and rectangular sandwich structures, indicating that such structures had excellent damage tolerance. The fracture behavior of the wave sandwich structure was slightly different from those of the other three ones. Although the wave sandwich structure also had specific damage tolerance and fracture toughness, its crushing behavior exhibited obvious shear fracture characteristics. Based

on the FEM analysis and the fracture morphology analysis of the wave sandwich structure, the crack propagation path of the sample under *Y*-axis compression went from the top middle position to the bottom ends of both sides (the red dotted line in Fig. 8(d1)), and a non-crushed area was present in the wave sandwich structure (the blue triangular area in Fig. 8(d2)). In summary, the four specific bio-inspired sandwich structures possessed a series of intrinsic toughening mechanisms in the *Y*-axis direction of compression, and all the structures could ensure the effective transmission of internal stress when the sample was compressed.

Through the above FEM analysis, it can be confirmed that the compressive strength of each bio-inspired structure in the *Z*-axis direction was significantly higher than its compressive strength in the *Y*-axis direction. As shown in Fig. 9(a), the stress–strain curves corresponding to the four structures under the *Z*-axis direction compression indicated that each structure exhibited a similar ductile fracture behavior to that under crushing in the *Y*-axis direction. Notably, the compressive strength and the maximum strain in the

Z-axis direction of each structure were significantly increased compared to the strength in the *Y*-axis compression, as shown in Fig. 9(b). The compressive strengths of the honeycomb structure, the triangular structure, the wave structure, and the rectangular structure were 46.7, 26.5, 23.8, and 34.4 MPa, respectively. In the meantime, the maximum fracture strain of honeycomb structure, triangular structure, wave structure, and rectangular structure were 12.1%, 13.7%, 13.6%, and 13.9%, respectively. As shown in Figs. 9(c) and 9(d), when the sample undergoes *Z*-axis compression (in the case of honeycomb structures), its overall crushing would be accompanied by crack initiation at the side. Furthermore, it can be observed from the FEM analysis (Fig. 9(e)) that when the collapse occurred in the *Z*-axis direction, the stress transfer from top to bottom occurred in all structures. The compressive strengths of other state-of-the-art 3D-printed cement/geopolymer composites are summarized in Table 4. The relatively high compressive strength and toughness make 3D-printed LRS-1 GP with biomimetic sandwich patterns robust candidates for the construction of a Lunar base.
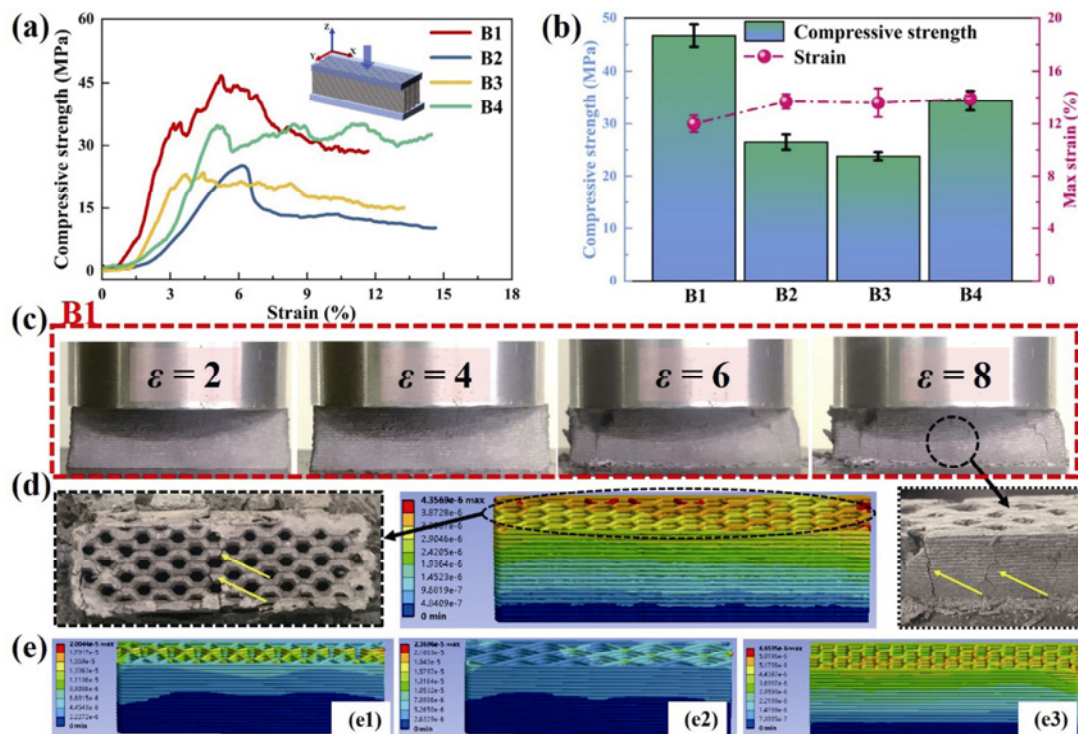

Fig. 9 Fracture mechanism analysis of honeycomb, triangular, wave, and rectangular sandwich structures under quasi-static crushing in *Z*-axis direction. (a) Stress–strain curves of the four sandwich structures during the *Z*-axis compression test. (b) Comparison of compressive strength and maximum strain for the four patterns in *Z*-axis direction compression. (c) Photographs of the samples with honeycomb sandwich patterns at different stages of the compression test (ε is the strain). (d) Photograph of fractured honeycomb sandwich structure and local stress analysis of honeycomb sandwich pattern during *Z*-axis compression. (e) Local stress analysis of triangular, wave, and rectangular sandwich structures during *Z*-axis compression by the FEM.

Table 4 Comparison of compressive strength of cement/geopolymer composites with different structures and molding processes

Material	Curing time (d)	Structure	Compressive strength (MPa)	Ref.
Cast GP–Lunar simulants	28	Bulk	0.7–2.5	[5]
3D-printed honeycomb composites	—	Honeycomb	6–10	[11]
3D-printed cement-based composites	28	Column	30–60	[57]
3D-printed GP-based composites	7	Cube	16.5	[58]
3D-printed sand/geopolymer	7	Rectangular	18.4	[59]
3D-printed concrete column	28	Column	38.3–68.6	[60]
3D-printed geopolymer concrete	7	Column	22–35	[61]
$1C_{sf}$/20QS@HIT-LRS-1 GP (*Y*-axis)	9	Cellular	11.3–20.1	This work
$1C_{sf}$/20QS@HIT-LRS-1 GP (*Z*-axis)	9	Cellular	23.8–46.7	This work

For this study, the Lunar base construction is still in the validation stages. Therefore, the follow-up research will focus on the 3D printing of Lunar regolith simulant-based geopolymers under low gravity environments, changing the type of fibers (such as basalt fibers) as the reinforcement, determining the durability of geopolymers under freezing cycles, and improving the thermal insulation of printed products through structural design.

4 Conclusions

In conclusion, we demonstrated successful 3D printing of C_{sf}/QS@HIT-LRS-1 based GP composites with different plant-inspired biomimetic sandwich patterns and elucidated the pattern-dependent fracture mechanisms by combining compression tests and the FEM analysis. The developed $1C_{sf}$/20QS@HIT-LRS-1 GP ink showed excellent rheological properties, such as high shear initial viscosity of ~33,279 Pa and high shear yield stress (τ_0) of ~8628 Pa, enabling DIW of $1C_{sf}$/20QS@HIT-LRS-1 composites with high spatial resolution. Meanwhile, by carefully tuning the ratio of L to nozzle diameter, C_{sf} showed preferred alignment parallel to the extrusion direction, thereby enhancing the mechanical properties of the specimen via pull-out. When the carbon fiber content in the sample was 1.00 vol%, the flexural strength of the corresponding $1C_{sf}$/20QS@HIT-LRS-1 GP sample reached the maximum of 41.6 MPa, increased by 50.7% compared to that of the composite without carbon fibers. Furthermore, all the bio-inspired structures exhibited anisotropic mechanical properties, i.e., the compressive strength in the *Z*-axis direction was significantly higher than that in the *Y*-axis direction. The compressive strengths of

the 3D-printed C_{sf}/QS@HIT-LRS-1 composites in *Z*-axis direction with honeycomb, triangular, wave, and rectangular sandwich patterns were found to be 46.7, 26.5, 23.8, and 34.4 MPa, respectively, vastly outperforming most other 3D-printed cement- and geopolymer-based materials with various architectures. Furthermore, in addition to exhibiting an excellent compressive strength, each structure exhibited stable non-catastrophic failure characteristics upon fracture and impact protection capacity. Our results offer an alternative approach to fabricate high-quality C_{sf}/QS@HIT-LRS-1 GP composites and provide new insights into tuning their mechanical properties and crashworthiness for advanced applications.

Declaration of competing interest

The authors have no competing interests to declare that are relevant to the content of this article.

References

[1] Karl D, Cannon KM, Gurlo A. Review of space resources processing for Mars missions: Martian simulants, regolith

bonding concepts and additive manufacturing. *Open Ceramics* 2022, **9**: 100216.

[2] Gellert R, Rieder R, Anderson RC, *et al*. Chemistry of rocks and soils in Gusev Crater from the alpha particle X-ray spectrometer. *Science* 2004, **305**: 829–832.

[3] Wang KT, Tang Q, Cui XM, *et al*. Development of near-zero water consumption cement materials via the geopolymerization of tektites and its implication for Lunar construction. *Sci Rep* 2016, **6**: 29659.

[4] Ferrone KL, Taylor AB, Helvajian H. *In situ* resource utilization of structural material from planetary regolith. *Adv Space Res* 2022, **69**: 2268–2282.

[5] Alexiadis A, Alberini F, Meyer ME. Geopolymers from Lunar and Martian soil simulants. *Adv Space Res* 2017, **59**: 490–495.

[6] Mills JN, Katzarova M, Wagner NJ. Comparison of Lunar and Martian regolith simulant-based geopolymer cements formed by alkali-activation for *in-situ* resource utilization. *Adv Space Res* 2022, **69**: 761–777.

[7] Moroz LV, Basilevsky AT, Hiroi T, *et al*. Spectral properties of simulated impact glasses produced from Martian soil analogue JSC Mars-1. *Icarus* 2009, **202**: 336–353.

[8] Isachenkov M, Chugunov S, Smirnov A, *et al*. The effect of particle size of highland and mare Lunar regolith simulants on their printability in vat polymerisation additive manufacturing. *Ceram Int* 2022, **48**: 34713–34719.

[9] Rattanasak U, Chindaprasirt P. Influence of NaOH solution on the synthesis of fly ash geopolymer. *Miner Eng* 2009, **22**: 1073–1078.

[10] Compton BG, Lewis JA. 3D-printing of lightweight cellular composites. *Adv Mater* 2014, **26**: 5930–5935.

[11] Cheng YY, Li JJ, Qian XP, *et al*. 3D printed recoverable honeycomb composites reinforced by continuous carbon fibers. *Compos Struct* 2021, **268**: 113974.

[12] Ortiz C, Boyce MC. Bioinspired structural materials. *Science* 2008, **319**: 1053–1054.

[13] Arunothayan AR, Nematollahi B, Ranade R, *et al*. Fiber orientation effects on ultra-high performance concrete formed by 3D printing. *Cement Concrete Res* 2021, **143**: 106384.

[14] Alomayri T. Performance evaluation of basalt fiber-reinforced geopolymer composites with various contents of nano $CaCO_3$. *Ceram Int* 2021, **47**: 29949–29959.

[15] Korniejenko K, Łach M. Geopolymers reinforced by short and long fibres—Innovative materials for additive manufacturing. *Curr Opin Chem Eng* 2020, **28**: 167–172.

[16] Lin TS, Jia DC, He PG, *et al*. Effects of fiber length on mechanical properties and fracture behavior of short carbon fiber reinforced geopolymer matrix composites. *Mater Sci Eng A* 2008, **497**: 181–185.

[17] Yan S, He PG, Jia DC, *et al*. Crystallization kinetics and microstructure evolution of reduced graphene oxide/geopolymer composites. *J Eur Ceram Soc* 2016, **36**: 2601–2609.

[18] Song CL, Jin XL. Analytical modeling of chip formation mechanism in cutting unidirectional carbon fiber reinforced polymer. *Compos Part B-Eng* 2022, **239**: 109983.

[19] Hanaoka T, Ikematsu H, Takahashi S, *et al*. Recovery of carbon fiber from prepreg using nitric acid and evaluation of recycled CFRP. *Compos Part B-Eng* 2022, **231**: 109560.

[20] Yuan JK, He PG, Jia DC, *et al*. SiC fiber reinforced geopolymer composites, Part 1: Short SiC fiber. *Ceram Int* 2016, **42**: 5345–5352.

[21] Ma SQ, He PG, Zhao SJ, *et al*. Formation of SiC whiskers/leucite-based ceramic composites from low temperature hardening geopolymer. *Ceram Int* 2021, **47**: 17930–17938.

[22] Ma SQ, Zhao SJ, Zheng Y, *et al*. Preparation and mechanical performance of SiC_w/geopolymer composites through direct ink writing. *J Am Ceram Soc* 2022, **105**: 3555–3567.

[23] Chen Z, Sun XH, Shang YP, *et al*. Dense ceramics with complex shape fabricated by 3D printing: A review. *J Adv Ceram* 2021, **10**: 195–218.

[24] Assaedi H, Alomayri T, Shaikh FUA, *et al*. Characterisation of mechanical and thermal properties in flax fabric reinforced geopolymer composites. *J Adv Ceram* 2015, **4**: 272–281.

[25] Naleway SE, Porter MM, McKittrick J, *et al*. Structural design elements in biological materials: Application to bioinspiration. *Adv Mater* 2015, **27**: 5455–5476.

[26] Zhang MY, Zhao N, Yu Q, *et al*. On the damage tolerance of 3-D printed Mg–Ti interpenetrating-phase composites with bioinspired architectures. *Nat Commun* 2022, **13**: 3247.

[27] Jia ZA, Wang LF. 3D printing of biomimetic composites with improved fracture toughness. *Acta Mater* 2019, **173**: 61–73.

[28] Huang W, Restrepo D, Jung JY, *et al*. Multiscale toughening mechanisms in biological materials and bioinspired designs. *Adv Mater* 2019, **31**: 1901561.

[29] Siddique SH, Hazell PJ, Wang HX, *et al*. Lessons from nature: 3D printed bio-inspired porous structures for impact energy absorption—A review. *Addit Manuf* 2022, **58**: 103051.

[30] Moini M, Olek J, Youngblood JP, *et al*. Additive manufacturing and performance of architectured cement-based materials. *Adv Mater* 2018, **30**: 1802123.

[31] Gibson LJ. The hierarchical structure and mechanics of plant materials. *J R Soc Interface* 2012, **9**: 2749–2766.

[32] Palombini FL, de Araujo Mariath JE, de Oliveira BF. Bionic design of thin-walled structure based on the geometry of the vascular bundles of bamboo. *Thin Wall Struct* 2020, **155**: 106936.

[33] Peng MW, Wen Z, Xie LJ, *et al*. 3D printing of ultralight biomimetic hierarchical graphene materials with exceptional stiffness and resilience. *Adv Mater* 2019, **31**: 1902930.

[34] Yazdani Sarvestani H, Akbarzadeh AH, Niknam H, *et al*. 3D printed architected polymeric sandwich panels: Energy absorption and structural performance. *Compos Struct* 2018, **200**: 886–909.

[35] Zhang BX, Xiang MJ, Zhang Q, *et al*. Preparation and characterization of bioinspired three-dimensional architecture of zirconia on ceramic surface. *Compos Part B-Eng* 2018, **155**: 77–82.

[36] Ray CS, Reis ST, Sen S, *et al*. JSC-1A Lunar soil simulant: Characterization, glass formation, and selected glass properties. *J Non Cryst Solids* 2010, **356**: 2369–2374.

[37] Bish DL, Blake DF, Vaniman DT, *et al*. X-ray diffraction results from Mars Science Laboratory: Mineralogy of rocknest at Gale crater. *Science* 2013, **341**: 1238932.

[38] Xiong GY, Guo XL, Yuan ST, *et al*. The mechanical and structural properties of Lunar regolith simulant based geopolymer under extreme temperature environment on the moon through experimental and simulation methods. *Constr Build Mater* 2022, **325**: 126679.

[39] UOCF. LHS-1 Lunar highlands simulant, 2021. Available at https://sciences.ucf.edu/class/simulant_lunarhighlands.

[40] Collins PJ, Edmunson J, Fiske M, *et al*. Materials characterization of various Lunar regolith simulants for use in geopolymer Lunar concrete. *Adv Space Res* 2022, **69**: 3941–3951.

[41] Wang KT, Lemougna PN, Tang Q, *et al*. Lunar regolith can allow the synthesis of cement materials with near-zero water consumption. *Gondwana Res* 2017, **44**: 1–6.

[42] Taylor GJ, Martel LMV, Lucey PG, *et al*. Modal analyses of Lunar soils by quantitative X-ray diffraction analysis. *Geochim Cosmochim Ac* 2019, **266**: 17–28.

[43] Zocca A, Fateri M, Al-Sabbagh D, *et al*. Investigation of the sintering and melting of JSC-2A Lunar regolith simulant. *Ceram Int* 2020, **46**: 14097–14104.

[44] Engelschiøn VS, Eriksson SR, Cowley A, *et al*. EAC-1A: A novel large-volume Lunar regolith simulant. *Sci Rep* 2020, **10**: 5473.

[45] Ma SQ, Fu S, Zhao SJ, *et al*. Direct ink writing of geopolymer with high spatialresolution and tunable mechanical properties. *Addit Manuf* 2021, **46**: 102202.

[46] Yang LL, Zeng XJ, Ditta A, *et al*. Preliminary 3D printing of large inclined-shaped alumina ceramic parts by direct ink writing. *J Adv Ceram* 2020, **9**: 312–319.

[47] Zhao Z, Zhou GX, Yang ZH, *et al*. Direct ink writing of continuous SiO_2 fiber reinforced wave-transparent ceramics. *J Adv Ceram* 2020, **9**: 403–412.

[48] Zawrah MF, Farag RS, Kohail MH. Improvement of physical and mechanical properties of geopolymer through addition of zircon. *Mater Chem Phys* 2018, **217**: 90–97.

[49] Guo XL, Yang JY, Xiong GY. Influence of supplementary cementitious materials on rheological properties of 3D printed fly ash based geopolymer. *Cement Concrete Comp* 2020, **114**: 103820.

[50] Franchin G, Scanferla P, Zeffiro L, *et al*. Direct ink writing of geopolymeric inks. *J Eur Ceram Soc* 2017, **37**: 2481–2489.

[51] Kanarska Y, Duoss EB, Lewicki JP, *et al*. Fiber motion in highly confined flows of carbon fiber and non-Newtonian polymer. *J Non-Newton Fluid* 2019, **265**: 41–52.

[52] Perez M, Scheuer A, Abisset-Chavanne E, *et al*. A multi-scale description of orientation in simple shear flows of confined rod suspensions. *J Non-Newton Fluid* 2016, **233**: 61–74.

[53] Sajadi SM, Boul PJ, Thaemlitz C, *et al*. Direct ink writing of cement structures modified with nanoscale additive. *Adv Eng Mater* 2019, **21**: 1801380.

[54] Chabi S, Rocha VG, García-Tuñón E, *et al*. Ultralight, strong, three-dimensional SiC structures. *ACS Nano* 2016, **10**: 1871–1876.

[55] Farrokhabadi A, Mahdi Ashrafian M, Behravesh AH, *et al*. Assessment of fiber-reinforcement and foam-filling in the directional energy absorption performance of a 3D printed accordion cellular structure. *Compos Struct* 2022, **297**: 115945.

[56] Zhang XQ, Zhang KQ, Zhang L, *et al*. Additive manufacturing of cellular ceramic structures: From structure to structure–function integration. *Mater Design* 2022, **215**: 110470.

[57] Xu ZY, Zhang DW, Li H, *et al*. Effect of FA and GGBFS on compressive strength, rheology, and printing properties of cement-based 3D printing material. *Constr Build Mater* 2022, **339**: 127685.

[58] Xia M, Sanjayan J. Method of formulating geopolymer for 3D printing for construction applications. *Mater Design* 2016, **110**: 382–390.

[59] Panda B, Unluer C, Tan MJ. Investigation of the rheology and strength of geopolymer mixtures for extrusion-based 3D printing. *Cement Concrete Comp* 2018, **94**: 307–314.

[60] Zhu BR, Nematollahi B, Pan JL, *et al*. 3D concrete printing of permanent formwork for concrete column construction. *Cement Concrete Comp* 2021, **121**: 104039.